Advanced Powder Materials 5 (2026) 100369

Contents lists available at ScienceDirect

Advanced Powder Materials

journal homepage: www.keaipublishing.com/en/journals/advanced-powder-materials

Ultrastrong and ductile hierarchical heterostructured titanium composites from room to high temperatures

Shaolong Li[a,b], Shufeng Li[a,*], Huiying Liu[a], Lei Liu[a], Shaodi Wang[a], Dongxu Hui[a], Jie Yan[b], Rui zhou[b], Dingbo Tao[a], Wenfei Huang[a], Jianbo Gao[c], Xiaodong Hou[d], Xin Zhang[a], Bo Li[a], Zhimao Wang[e], Gang Li[e], Junhua Luan[b], Junko Umeda[f], Katsuyoshi Kondoh[f], Philip J. Withers[g,**], Yuntian Zhu[b,***]

[a] School of Materials Science and Engineering, Xi'an University of Technology, Xi'an 710048, China
[b] Department of Materials Science and Engineering, City University of Hong Kong, Hong Kong, China
[c] Centre of Excellence for Advanced Materials, Dongguan 523808, China
[d] Division of Mechanics and Acoustics, National Institute of Metrology, Beijing 100013, China
[e] Institute of High Energy Physics, Chinese Academy of Sciences, Beijing 100049, China
[f] Joining and Welding Research Institute, Osaka University, Ibaraki, Osaka, 567-0047, Japan
[g] Henry Royce Institute, Department of Materials, University of Manchester, Manchester, M13 9PL, UK

ARTICLE INFO

Keywords:
Heterostructure
Powder metallurgy
Titanium matrix composites
Strengthening–toughening mechanism
Mechanical properties

ABSTRACT

Titanium matrix composites (TMCs) offer significant enhancements in strength and heat resistance while preserving the low-density characteristic of advanced lightweight titanium alloys. However, ultra-strong, high-temperature TMCs are typically brittle at room temperature. Here, we overcome this limitation reporting a novel hierarchical, heterostructured design that achieving a 9.5% ductility —exceeding that of the TA15 matrix alloy—along with a remarkable tensile strength of nearly 1.4 GPa at room temperature and 700 MPa at 600 °C. This design forms hard, fine-grained regions homogeneously embedded within a soft, coarse-grained matrix. The hierarchical architecture facilitates the emergence of hetero-deformation-induced (HDI) stresses and strain partitioning, thereby enhancing strain hardening and dislocation activity. Our design strategy provides a pathway to achieving not only an optimal combination of strength-ductility at room-temperature but also exceptional high-temperature resistance.

1. Introduction

With global warming intensifying [1], there is an urgent need for lightweight, ultra strong and ductile structural materials that can perform across a wide temperature range in various industrial sectors. Such materials are critical for enhancing energy efficiency and the thrust-to-weight ratio in aerospace applications, as well as for reducing emissions in industrial production and transportation [2,3]. However, traditional structural materials often face limitations in practical engineering applications [3], including a narrow service temperature range [4–6], high cost [7,8], low elastic modulus [6], and restricted specific strength [5,7,8]. Examples include ordered intermetallic TiAl alloys [4], stainless steel [5], high-strength β-Ti alloys [6], nickel-based superalloys [8], and high-entropy alloys [7]. By contrast, titanium matrix composites (TMCs) exhibit exceptional potential in structural engineering due to their superior strength-to-weight ratio at room temperature—the highest among all metals—combined with outstanding high-temperature mechanical properties [9–13]. Conventional TMCs with uniformly distributed reinforcements achieve ultra-high strength at elevated temperatures by effectively pinning grain boundaries and phase interfaces, but this comes at the expense of room-temperature ductility [10,14]. The primary cause of failure in uniform TMCs is stress concentration around the reinforcements, which leads to preferential crack nucleation within these phases and

* Corresponding author.
** Corresponding author.
*** Corresponding author.
E-mail addresses: shufengli@xaut.edu.cn (S. Li), p.j.withers@manchester.ac.uk (P.J. Withers), y.zhu@cityu.edu.hk (Y. Zhu).
Peer review under the responsibility of Central South University.

https://doi.org/10.1016/j.apmate.2025.100369
Received 11 August 2025; Received in revised form 21 October 2025; Accepted 26 October 2025
Available online 1 November 2025

subsequent rapid propagation, ultimately resulting in failure [10]. For instance, while the network architecture significantly improves the high-temperature mechanical performance of titanium matrix composites (TMCs), it also promotes rapid crack propagation along reinforcement-rich zones, often leading to premature failure. Currently, conventional single strengthening mechanisms, such as solid solution strengthening [15], precipitation strengthening [16], and dispersion strengthening [17] can significantly enhance high temperature strength but inevitably lead to reduced room-temperature ductility [4,10,16].

To improve ductility at room temperature in TMCs, a heterostructure strategy might be effective. Heterostructured materials (HSMs) have been reported to effectively mitigate the strength-ductility trade-off by leveraging hetero-deformation-induced (HDI) strengthening and HDI strain hardening, particularly at low homologous temperatures [9, 18–23]. The enhanced performance in heterogeneous structures originates from the mechanical interaction between soft and hard domains. This interplay promotes strain partitioning and induces substantial HDI stress, thereby effectively improving the work hardening capacity without compromising ductility. For example, a heterostructured Ti was found to be able to combine the high strength of ultrafine-grained Ti with the excellent ductility of coarse-grained Ti [18,19,23,24]. However, at elevated temperatures, HDI stress typically weakens due to easier dislocation recovery, which reduces dislocation pile-up, as well as diminished mechanical incompatibility [23]. Additionally, weakened bonding at heterogeneous interfaces and grain boundaries promotes interface and grain boundary sliding as primary deformation mechanisms, further compromising strength at high temperatures [17,25]. Currently, the challenge of achieving both ultra-high strength at elevated temperatures and high ductility at room temperature remains unresolved with existing methods and technologies.

2. Results and discussion

Here, we report a novel heterostructure Ti-6.5Al-2Zr-1Mo-1V-0.5Si-3.4TiB composite (wt.%), which is hereafter referred to as TA15-*Si*-TiB (Figs. S1 and S2) that exhibits exceptional mechanical performance across a broad temperature range. Scanning backscattered electron microscopy (BSE-SEM) (Fig. 1, a and a1) reveals a spherical heterostructure, 53–75 μm in diameter, consisting of TiB whiskers (TiBw) uniformly distributed within the matrix. This structure primarily forms through the reaction and mutual diffusion between spherical Ti-TiB prealloyed powders (Fig. S1) and aluminum [26]. Fig. S3 shows an electron probe microanalysis (EPMA) compositional image of the TA15-*Si*-TiB composite, showing whisker-like boron-enriched phases that self-assemble into spherical structures. These spheres, with a discontinuous TiBw distribution, are homogeneously embedded in the TA15 alloy matrix (Fig. 1, b), ensuring connectivity in the coarse-grained

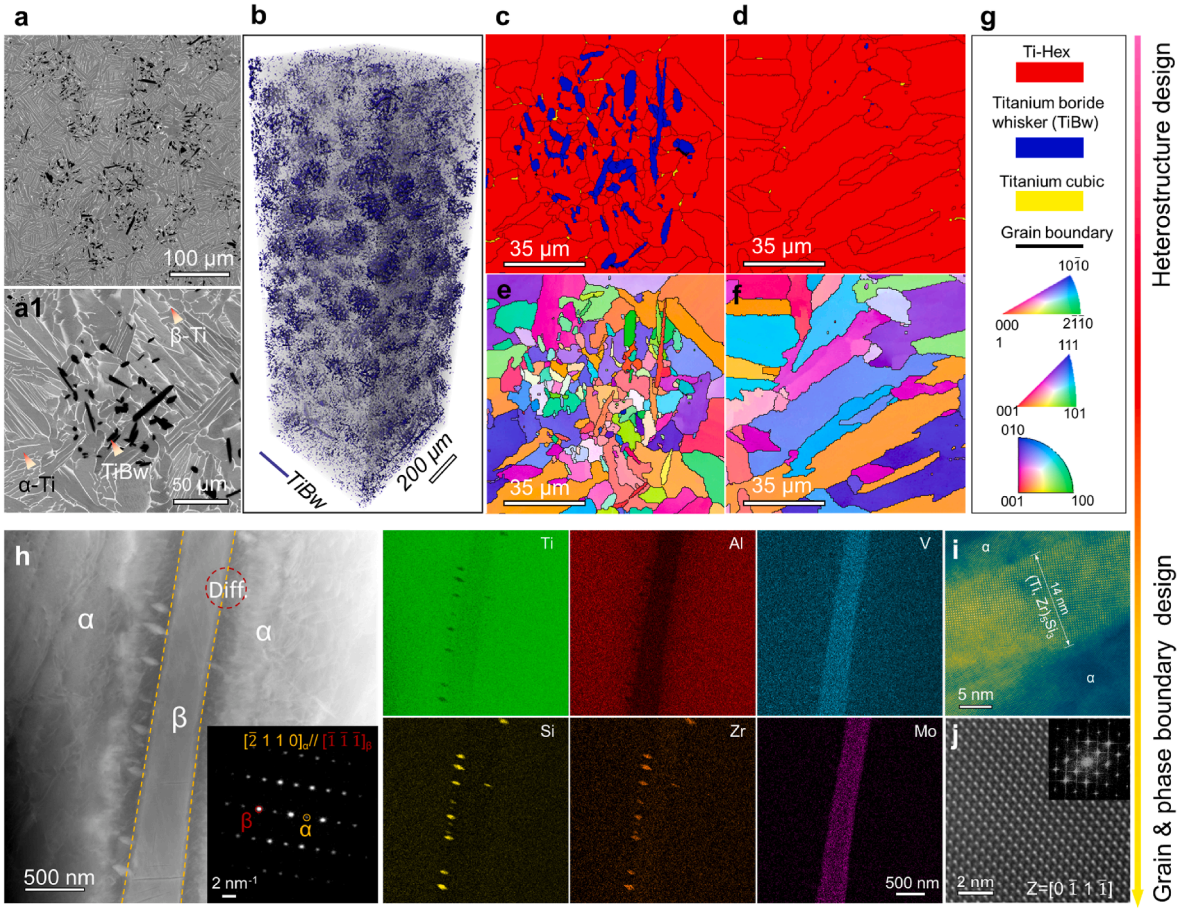

Fig. 1. Heterogeneous microstructure of the sintered TA15-*Si*-TiB composite. (a) BSE-SEM image of the sintered TA15-*Si*-TiB composite, showing the distribution of TiB within the matrix alloy; (a1) the locally magnified image of (a), with α phase, β phase, and TiB phase labeled. (b) Three-dimensional volume rendering of the sintered TA15-*Si*-TiB composite via high-energy synchrotron X-ray tomography, where blue represents TiBw, and the remaining zones correspond to the TA15-*Si* matrix. (c,d) EBSD phase maps of the TiBw-rich (hard) and TiBw-lean (soft) zones, respectively. (e,f) EBSD inverse pole figure (IPF) maps corresponding to the TiBw-rich and TiBw-lean zones. (g) Legend for (c) to (f). (h) HAADF-STEM image showing the matrix and nanoscale precipitates, with corresponding EDS mapping; the inset presents the SAED pattern corresponds to the α/β phase boundary. (i) Morphology and high-resolution image of the $(Ti,Zr)_5Si_3$ phase. (j) SAED pattern corresponding to (i).

zones. EPMA (Fig. S3), electron backscatter diffraction (EBSD) phase maps (Fig. 1c–f, and Fig. S4), and X-ray diffraction results (Fig. S5) confirm that the whisker-like phases are TiBw. The pinning effect of TiBw on matrix grains [27] results in a fine-grained zone (~5.7 μm, harder zones; Fig. 1c–e, Fig. S4) in TiBw-rich areas, while TiBw-lean areas develop coarse-grained zones (~28.4 μm, softer zones; Fig. 1d–f, Fig. S4). A nano-indentation load-displacement curve (Fig. S6) reveals a hardness gradient extending from the periphery to the interior of the TiBw spheres, leading to softer zones in TiBw-lean zones and hard zones in TiBw-rich zones. A high-angle annular dark-field scanning transmission electron microscopy (HAADF-STEM) image (Fig. 1, h) reveals the morphology and distribution of nano-precipitates, while selected area electron diffraction (SAED) patterns confirm a Burgers orientation relationship (BOR) between the α-Ti and β-Ti phases [11]. Energy-dispersive X-ray spectroscopy (EDS) maps identify Ti-, Zr-, and Si-rich precipitates at phase interfaces. Elemental mapping shows Al (red), an α-stabilizing element, along with Mo (purple) and V (cyan), β-stabilizing elements, confirming that the central strip is a β phase (BCC) flanked by α phases (HCP). High-resolution imaging and SAED analysis further determine the atomic distribution and lattice type of the nano-precipitates. Fig. 1, i shows cone-shaped precipitates (~14 nm wide and 47 nm long), which SAED patterns (Fig. 1, j) identify as hexagonal silicide S1 (Ti, Zr)$_5$Si$_3$ (a=0.780 nm; c=0.544 nm) located at phase boundaries [28]. Theoretical calculations indicate that the content of the in-situ precipitated nano-sized (Ti,Zr)$_5$Si$_3$ phase is approximately 2.44 wt%. Fig. S7 and S8 provide extended microstructural comparisons of different samples.

This study addresses the critical challenge of low high-temperature strength in conventional heterogeneous structures—caused by inadequate interfacial stability—through a novel multi-level heterogeneous structure design. This strategy not only achieves an optimal combination of room-temperature strength and ductility, but also leads to exceptional high-temperature strength, as clearly demonstrated in Fig. 2. Fig. 2, a and b display the engineering stress-strain curves of five representative samples tested at room temperature and 600 °C, respectively. The engineering stress-strain curves and mechanical properties of comparative samples are provided in Fig. S9. This study focuses on the TA15-*Si*-TiB composite, which exhibits an outstanding synergy of strength and ductility across a wide temperature range, achieved through grain boundary and heterostructure design. the TA15-*Si*-TiB composite achieves a yield strength (YS) of 1019 MPa with a ductility of 6.3%, demonstrating superior mechanical performance. More notably, after multi-directional forging, its yield strength increases to 1286 MPa—a 50% improvement over the TA15 alloy—while maintaining excellent ductility at 9.5%. The nearly flat post-peak stress-strain curves, indicative of a dynamic balance between work hardening and damage-induced

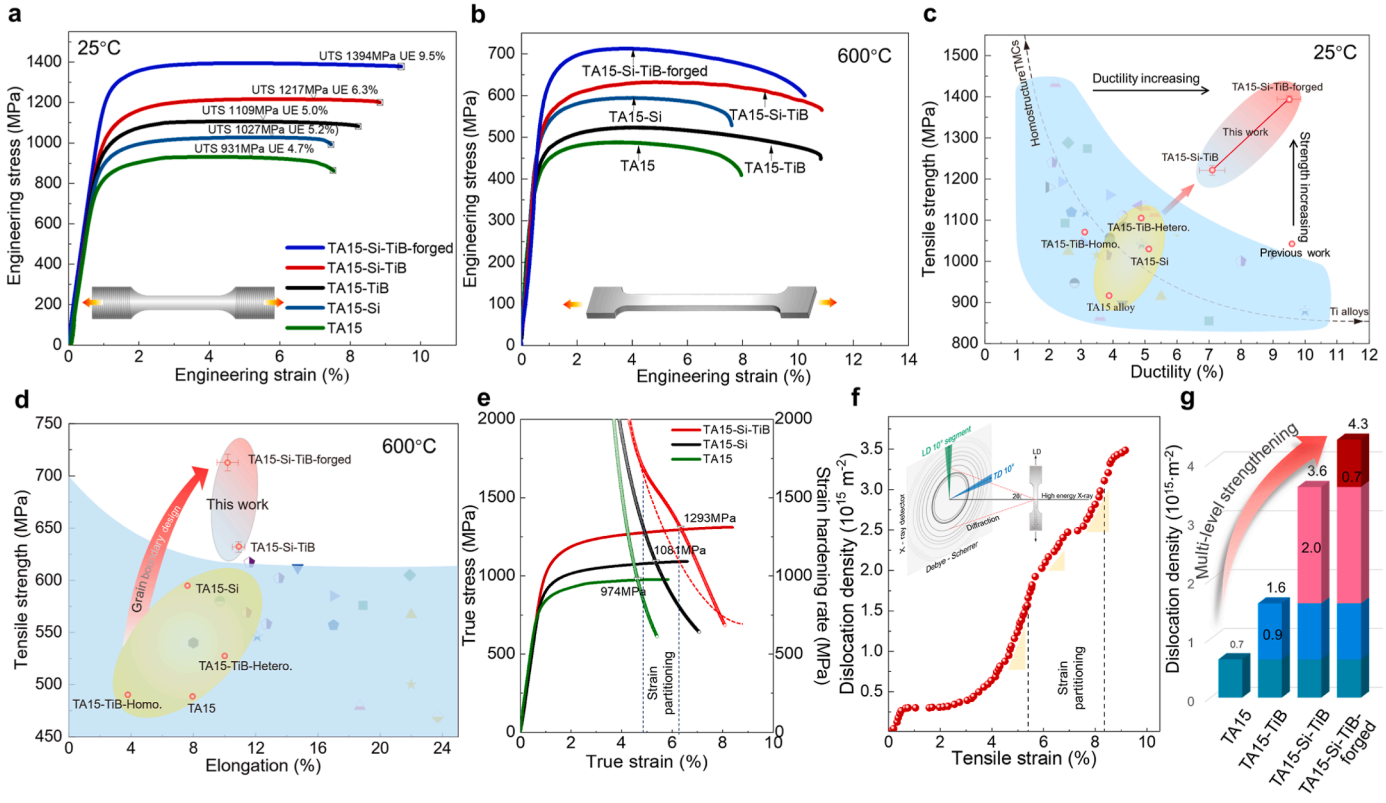

Fig. 2. Tensile mechanical properties and dislocation density during tension of TA15-*Si*-TiB composites. (a,b) Engineering stress–strain curves for five representative samples at 25 °C, and 600 °C, respectively. The triangle symbol marks the uniform elongation (UE) at the point of ultimate tensile strength (UTS). The inset in (a) illustrates the schematic of a dog-bone sample used for tensile tests at room temperature, while the inset in (b) depicts a similar schematic for high-temperature tensile tests. (c) Comparison of UTS and ductility balance with previously reported TMCs and near α-Ti alloys at room temperature. The blue zone represents traditional titanium alloys and homostructured TMCs. The yellow zone shows properties of comparable samples. The red gradient zone in the upper right highlights the performance of sintered TA15-*Si*-TiB and multi-directional forging TA15-*Si*-TiB composites (see detailed data and references in Table S4). (d) Plot of tensile strength versus elongation, comparing the strength–elongation trade-offs of traditional TMCs and high-temperature titanium alloys. Detailed data and references are provided in Table S5. (e) True stress–strain and strain-hardening rate curves for TA15, TA15-*Si*, and TA15-*Si*-TiB samples. The necking points are marked on the true stress–strain curves. A red dashed line illustrates the hypothetical extension of the strain-hardening rate curve trend for the TA15-*Si*-TiB sample. (f) Dislocation density as a function of tensile strain, derived from in-situ tensile SXRD measurements and the Williamson–Hall method. Inset: Schematic representation of the in-situ tensile SXRD test, showing integration along the loading direction (LD) from two-dimensional diffraction data. Corresponding one-dimensional diffraction and fitting curves are provided in Fig. S15. (g) Total dislocation density calculated based on the data presented in Fig. S16d.

softening, will be validated by quasi-in-situ SEM. Compared to conventional TMCs and near-α Ti alloys, the TA15-*Si*-TiB series composite exhibits significantly enhanced mechanical properties at room temperature (Fig. 2, c).

Unlike traditional processing techniques that often result in a severe strength-ductility trade-off (Fig. 2, c, figs. S9 and S10), TA15-*Si*-TiB composites effectively overcome this limitation. Moreover, the forged TA15-*Si*-TiB composite achieves the highest specific tensile strength and specific yield strength among all investigated materials, including high-strength β alloys [29], high-strength steels [5], and high-entropy alloys [30] (Fig. S11). High-temperature properties were further validated through tensile strength measurements across the same temperature range (Fig. 2, b, fig. S12a). Remarkably, the forged TA15-*Si*-TiB composite exhibits significantly higher yield strength and elongation than other samples, extending the service temperature by 150 °C beyond that of the TA15 alloy [25]. This innovative design not only delays high-temperature necking in TA15-*Si*-TiB but also enhances dimensional stability at elevated temperatures, as evidenced by a lower thermal expansion coefficient (Fig. S12b and S13). Overall, this lightweight heterostructured composite achieves an outstanding combination of exceptional high-temperature strength (Fig. 2, d) and an unprecedented strength-ductility synergy at room temperature (Fig. 2, c), significantly outperforming comparable composites and titanium alloys. To explore the origin of this remarkable strength-ductility synergy, we first used in-situ SXRD to visually reveal the unique strain partitioning behavior of the heterostructure.

The exceptional strength and ductility of TA15-*Si*-TiB composites are governed by their deformation mechanisms. Compared to the matrix alloy, the heterostructured TA15-*Si*-TiB induces additional HDI hardening through strain partitioning (Fig. 2, e and Fig. S14) [18,31] To elucidate the strengthening and hardening mechanisms of TA15-*Si*-TiB while minimizing the influence of thermal deformation, we performed in-situ tensile testing using synchrotron X-ray diffraction (SXRD) (Methods; inset in Fig. 2, f). During deformation, the dislocation density (ρ) increased from an initial 2.3×10^{14} m^{-2} to 1.58×10^{15} m^{-2} as strain partitioning commenced, further rising to 3.11×10^{15} m^{-2}. By the end of the hardening stage, ρ reached 3.6×10^{15} m^{-2} (Fig. 2f and g). This significant increase in dislocation density provides substantial dislocation hardening, as described by the Taylor equation, where τ is flow stress; α is a constant (0.3) [32]; μ is the shear modulus (43.2 GPa); b is Burgers vector length (2.95×10^{-10} m); ρ is dislocation density. Based on this relationship, the strengthening contribution of dislocations to the TA15-*Si*-TiB forged sample is estimated to be approximately 226 MPa.

The density of geometrically necessary dislocations (GNDs) serves as a key indicator for evaluating the HDI effect in heterogeneous structures. The generation of GNDs in the sample is directly related to strain gradients, which we subsequently quantified via EBSD and DIC analyses to evaluate the GND density (Fig. 3), thereby validating this hypothesis. The interactions between heterogeneous zones generate strain gradients at the heterogeneous boundaries (Fig. 3 and Fig. S17) [33]. The strain gradient is accommodated by the formation of GNDs [34–36]. The density of GNDs is estimated using classical strain gradient theory [36,

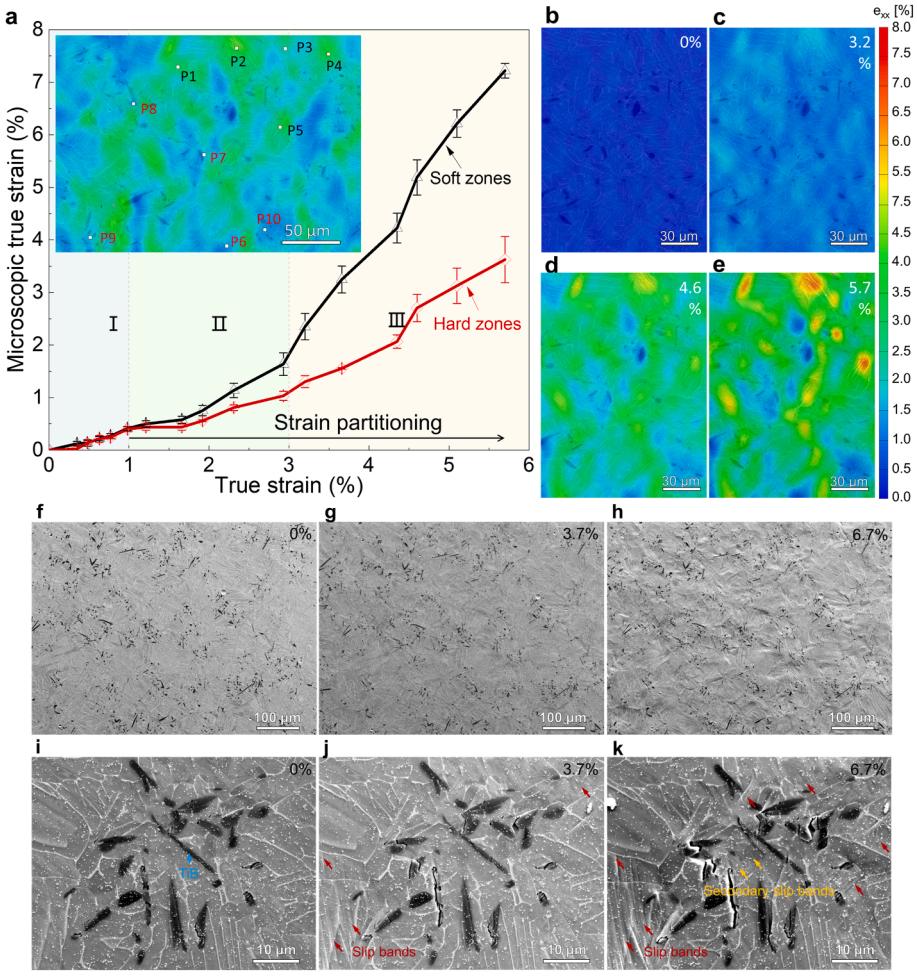

Fig. 3. Strain partitioning process and fracture mechanisms in the TA15-*Si*-TiB composite observed by digital image correlation (DIC) at room temperature. (a) Tensile strain-microscopic true strain curve at different stages. Inset: Strain distribution map of ε_x, with soft zones marked by black points and hard zones marked by red points. (b,e) Distribution of strain ε_x on the surface at 0, 3.2%, 4.6%, and 5.7% plastic strain. (f,h) Quasi-in situ tensile SEM snapshots capturing the evolution of the sample surface morphology at 0, 3.7%, and 6.7% true strain. (i,k) Strain partitioning process between the TiBw-rich and TiBw-lean zones at 0, 3.7%, and 6.7% true strain. Slip bands (marked by red arrows) are initially activated in the TiBw-lean zones.

37], as follows:, where ε the shear strain due to dislocation slip. Grain reference orientation deviation (GROD) maps from EBSD reveal a high strain gradient at the interfaces between hard and soft zones, promoting additional GNDs accumulation and extra strengthening (Fig. S17) [37]. The interconnected soft zones enable continuous strain transfer, preserving high ductility (Fig. 3a and Fig. S17). Moreover, strain partitioning from the soft to hard zones during deformation induces additional HDI strain hardening (Fig. 3b–e, and Fig. S17) [20,38]. As the GNDs density increases, the overall dislocation density in the sample also rises (Fig. 2, f). The entire strain process is divided into three stages. Stage I: Both the soft and hard zones exhibit similar elastic deformation capabilities. Stage II: The plastic deformation capability of the soft zones is enhanced, allowing them to accommodate larger strains relative to the hard zones during the plastic deformation process. Stage III: The strain capability of the soft zones increases compared to the previous stage, with strain being transferred to the hard zones, relieving stress concentration in these zones. The deformation in the hard zones leads to further hardening, delaying crack initiation. The plastic strain primarily occurs in the soft zones, which is crucial for maintaining ductility comparable to that of the matrix alloy.

In the soft zones, deformation accelerates the dislocation accumulation rate, reaching Peak 1 (Fig. 3, a; Stage I; Fig. S16). The accumulated strain leads to hardening in the soft zones, which is then transferred to the hard zones, causing the dislocation density to reach its second peak (Peak 2, Stage II). The alternating accumulation of dislocations and strain partitioning between the soft and hard zones effectively mitigates local strain concentration (Fig. 3, a). To investigate if this transformation mechanism is driven by the heterostructure or by phase transformation, we conducted SXRD investigations across the full azimuthal range for different planes near the necking zone (Fig. S17c). No new diffraction lines were observed, indicating that the strain partitioning during loading is not due to phase transformation [20]. Additionally, we performed SXRD tests on the necking zone of the TA15-*Si*-TiB composite and its comparative samples (Fig. S16 and d) to assess the contribution of the heterostructure and nanoscale particles to dislocation density (Fig. 2, g). The nanoscale (Ti, Zr)$_5$Si$_3$ phase enhances resistance to dislocation motion, thereby inducing extra dislocation strengthening [15,39].

Dislocation is critical for material strengthening, while crack tolerance is key to toughening. To investigate the mechanisms governing crack tolerance, we conducted quasi-in situ characterization of the microcrack evolution process within the spheroidal structure (Fig. 3 and Fig. S18–S19). Initially, slip traces appeared on the polished surface—these linear, localized shear regions were activated by a high Schmid factor [40]. As strain accumulated, alternating slip traces transitioned from coarse-grained to fine-grained regions, promoting secondary strain development (Fig. 3i–k) [41]. Subsequently, microcracks formed within the TiBw; however, their propagation was restricted by the surrounding fine-grained regions (Fig. 3i–k). The coarse-grained regions acted as a buffering layer, enhancing the material's ability to accommodate microcracks [20]. This crack propagation mode alleviates stress concentration at phase boundaries and reduces stress intensity at the tips of larger microcracks [20]. In the absence of these surrounding soft regions, cracks would propagate rapidly—akin to a "hot knife through butter"—ultimately causing premature failure. The presence of high-density microcracks and multi-stage slip mechanisms helps dissipate local stress concentrations [9]. By integrating coarse and fine grains to hinder crack propagation, we effectively delay necking and final failure (Stage III, Fig. 3, k). This heterostructure is crucial for maintaining an elongation comparable to that of the matrix while achieving enhanced ductility.

Slip bands are the physical evidence of dislocation-mediated plasticity. The initiation and propagation of slip bands mark the yield point of a crystal. Furthermore, the interaction of dislocations within and between developing slip bands is a primary contributor to work hardening. To further elucidate the micro mechanisms underpinning uniform plastic deformation at both room and high temperatures, we conducted an in-depth analysis of dislocations and elements in samples. We employed standard $g{\cdot}b$ analysis to identify the dislocation types, where g represents the diffraction vector and b denotes the Burgers vector (Table S6) [42]. A significant accumulation of dislocations was observed around the TiB phase (Fig. 4, a), contributing to the strengthening and hardening effect [15]. Additionally, a large number of <a>-type dislocations with b_1=1/3 <11 $\bar{2}$ 0> were activated (Fig. S20), facilitating pronounced plastic deformation along the <a>-axis. This is because the critical shear stress (CRSS) for <a+c> slip is much higher than that for <a> slip [43]. A small number of <c+a>-type dislocations with b_2=1/3 (11 $\bar{2}$ 3) were induced by nano (Ti, Zr)$_5$Si$_3$ particles (Fig. 4, b and Fig. S20). Notably, some <c+a> dislocations within the matrix slip in a planar mode, with many originating from the grain boundaries. The "bow-out" shape of <c+a> dislocations at the grain boundaries supports this observation, as these dislocations accommodate plastic strain along the <c>-axis (Fig. 4, b) [42,44]. Due to the Burgers orientation relationship (BOR) between the variant α phase and the parent β phase [11], dislocations can pass through dislocation entanglement in the α phase to further improve the strength of the sample (Fig. 4, c). The β phase reduces the local stress concentration caused by dislocation pile-up (Fig. 4, b and d). Notably, only a few straight dislocations exhibit a screw character, while the remaining curved mixed dislocations and edge dislocations demonstrate low migration rates and stability [45]. This allows them to maintain a high density even at elevated temperatures, thereby contributing to high-temperature strengthening [42,44,46].

In fact, numerous nanoscale (Ti, Zr)$_5$Si$_3$ particles are observed within the β phase, significantly enhancing its strength by inducing extra dislocation strengthening (Fig. S21) [47]. The accumulation of intra-granular dislocations facilitates slip and cross-slip of dislocations along the ($\bar{1}$ 10$\bar{1}$) plane, increasing the likelihood of cross-slip and promoting plastic strain delocalization (Fig. 4, d and Fig. S22b) [48]. This provides a sustained mechanism for plastic deformation, contributing to strain hardening and improved ductility [40,49]. Additionally, the TA15-*Si*-TiB composite exhibits enhanced ductility through shear deformation of the β phase (Fig. 4, d and Fig. S22b), further enhancing its ductility [50].

We also analyzed the high-temperature tensile strengthening mechanisms. Significant dislocation accumulation was observed in zones pinned by the TiBw and (Ti,Zr)$_5$Si$_3$ phases. The high dislocation density in these zones provides substantial strength at elevated temperatures (Fig. S23). The (Ti, Zr)$_5$Si$_3$ phase, present both at interfaces and within the β phase (Figs. S21 and S23), not only enhances grain boundary strength but also reinforces the β phase itself. Our APT data future revealed that Si is notably enriched at the α/β phase interfaces (Fig. 4e–g). Zr, Mo, and V are enriched in the β phase, while Al and Ti are correspondingly depleted. The strengthened heterogeneous interfaces facilitate dislocation strengthening as the dominant mechanism, enabling dislocation strengthening even at elevated temperatures. This unique interplay of mechanisms highlights the composite's remarkable ability to maintain strength and ductility across a wide temperature range.

3. Conclusion

In summary, a heterogeneous TA15-*Si*-TiB composite has been successfully designed, exhibiting an exceptional synergy of ultra-high strength and ductility from room to high temperatures. The experimental results demonstrate that the interconnected coarse-grained zones, formed via grain boundaries, impart the heterogeneous TA15-*Si*-TiB composites with high ductility at room temperature. Crucially, the interactions between the soft and hard zones induce extra strain partitioning processes, delaying crack initiation and propagation while

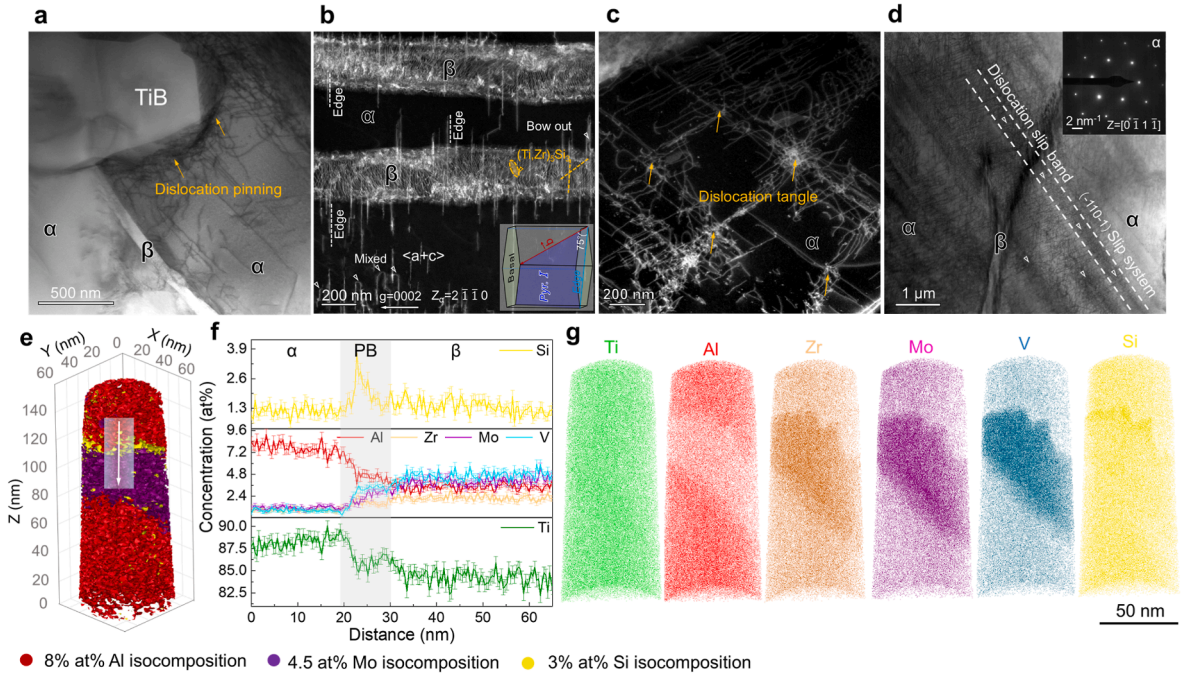

Fig. 4. Room and high temperature strengthening mechanism of TA15-*Si*-TiB composites. (a) Dark-field (DF) TEM image showing a dislocation pinned by TiB phase. (b) Under the double beam condition with *g*=0002, the DF-TEM image reveals a significantly higher density of activated <c+a> − type dislocations. Most of the <c+a> − type dislocations are preferentially aligned along the intersection line of the first-order pyramidal plane and the basal plane in the TA15-*Si*-TiB; predominantly exhibiting near-edge components, as confirmed by the schematic diagram. (c) DF-TEM image showing dislocation interactions in α-Ti. (d) Bright-field (BF) TEM image showing a significant accumulation of dislocations between α and β phases, with dislocations observed to slip through the β phase. Inset: SAED pattern corresponding to the α phase. (e) Three-dimensional atom probe tomography (3D-APT) reconstructions with iso-composition surfaces for 8 at% Al, 3 at% Si, and 4.5 at% Mo, revealing the morphologies of the α and β phases and interfacial nanoprecipitates. (f) One-dimensional compositional profile quantitatively illustrating the elemental distributions across the α and β phases. (g) Atom maps reconstructed from 3D-APT, displaying the distribution of each element.

facilitating sustained hardening. A breakthrough was achieved by incorporating spherical TiB clusters (hundreds of micrometers in size), which dramatically improve mechanical properties at both room and elevated temperatures without compromising the ductility level of the matrix. Furthermore, nanoscale precipitates at heterogeneous interfaces not only strengthen the β phase but also enhance grain boundary cohesion. These precipitates significantly impede dislocation motion at high temperatures, contributing to outstanding high-temperature performance.

Room-temperature performance primarily benefits from the strain gradient of the heterogeneous structure and HDI stress, whereas the retention of high-temperature performance may rely more on the pinning effect of nano-precipitates on grain/phase boundaries and their strong hindrance to dislocation motion. The coupling of HDI (at the hundred-micrometer scale) with nanoscale dislocation strengthening enables a synergistic enhancement of mechanical performance across room and high temperatures. This innovative strategy can be applied to other alloy systems, paving the way for advanced structural applications.

4. Material and methods

4.1. Material preparation and processing

Firstly, TiBw was generated via the reaction: $Ti+TiB_2 \rightarrow 2TiB$. A Ti–TiB pre-alloy ingot was produced by melting 98 wt% sponge titanium and 2 wt% TiB_2, followed by multiple melting and forging steps. Using electrode induction atomization technology, spherical Ti-TiB pre-alloy powder was prepared [9,51]. The selected Ti-3.4 wt% TiB pre-alloy powder had a particle size range of 53–75 μm. This powder was evenly mixed with 6.5 wt% Al, 2 wt% Zr, 1 wt% Mo, 1 wt% V, and 0.5 wt % Si (all with 99.9% purity, supplied by Avimetal Powder Metallurgy Technology Co., Ltd., China). The mixture was ball milled using zirconia balls as the milling medium, with a ball-to-material ratio of 5:1 and a speed of 250 rpm for 4 h. After milling, the powder mixture was dried in an oven at 60 °C for 2 h, then filled into a graphite mold for pre-pressing. The mold had an inner diameter of 30 mm and a height of 100 mm. The pre-pressed mixture was sintered by spark plasma using a SPS-1030S system at 1300 °C, under a pressure of 30 MPa, for 60 min. This process resulted in a cylindrical sample with dimensions Φ30×50 mm. The samples were cooled to room temperature within the furnace. For details on the sintering process and subsequent thermal treatments, refer to Fig. S2.

4.2. Room and high temperature mechanical test

Uniaxial tensile and loading–unloading–reloading (LUR) tests [52] were performed at room temperature using an AGS-X universal tensile testing machine (ZhongJi, China) at a strain rate of 5.0×10^{-4} s^{-1}. The tensile samples, with a cross-sectional diameter of Φ3 mm and a gauge length of 15 mm, were prepared from sintered and forged composites by electrical discharge machining. Elongation measurements were conducted using an extensometer. High-temperature tensile tests were conducted at 600 °C and 650 °C. The samples were machined into standard flat dog-bone-shaped samples with dimensions of 3 mm×2 mm and a gauge length of 26 mm. Sample surfaces were polished prior to testing. A tensile rate of 0.5 mm/min was applied using an Instron-45582 electronic universal tensile testing machine equipped with an electric resistance wire heating system and a high-temperature extensometer. Samples were heated in a resistance furnace and held at the target temperature for 20 min to ensure uniform temperature distribution. For all mechanical tests, the reported data represent the

average of at least three measurements. The microhardness distribution of TA15-*Si*-TiB, comprising soft and hard zones, was evaluated using quasi-static nanoindentation. Tests were conducted with a Nano-Indenter G200 machine in constant load mode. A 10× 2 point grid was applied across the soft and hard zones. The load was applied at a rate of 0.5 nm/s up to 50 mN, followed by a 10-s holding time. SEM imaging was used to characterize the indentation morphologies (Fig. S6). For a schematic representation of the experimental procedure, refer to Fig. S2.

4.3. Microstructure characterization

All tensile samples and Ti-TiB pre-alloy materials were polished with 200–2000 grit sandpaper prior to testing. Samples for optical microscopy were etched with Kroll's reagent to reveal grain and phase boundaries. Light optical microscopy (GX71; OLYMPUS, Japan) was employed to examine the microstructure. Microstructure and fracture morphology were analyzed using SEM (JEOL JSM-IT800, Japan) in secondary electron mode. Crystallographic information, including grain size and orientation distribution, was investigated using an EBSD system (Symmetry S2, OXFORD AZTEC; UK) integrated with a field-emission SEM (FESEM). The EBSD data were collected at an operating voltage of 20 kV. Prior to EBSD analysis, samples were chemically polished for 20 s at 30 V using an electrolyte containing 94% CH_3COOH and 6% $HClO_4$. EBSD data were analyzed with Channel 5 software. High-resolution STEM (Talos F200X) was used to characterize sintered samples and fracture surfaces. In-situ SEM observations were conducted on a JSM-IT800 field-emission SEM at 20 kV. In-situ SEM, EBSD, and digital image correlation (DIC) experiments were performed at a loading rate of 1 mm/min using SEM equipment equipped with an in-situ loading platform (Kammrath & Weiss GmbH) and a heating system. Tensile samples for room-temperature and high-temperature in-situ tests had cross-sectional dimensions of 1×3 mm^2 and a gauge length of 6 mm. High-temperature tensile tests involved heating the samples to the target temperature at a rate of 50 °C/min, followed by a 20-min hold to minimize temperature fluctuations and ensure uniform heating before loading. During testing, the crosshead could be paused at any time to observe microstructural evolution, with SEM imaging performed on the zone of interest. In DIC experiments, speckles were created using SiO_2 suspension. The sample surface was polished to a mirror finish, and 5 mL of SiO_2 suspension (particle size 20–50 nm) was applied to a polishing cloth. The sample was pressed with ~5 kg force and rotated in alternating directions. After eight rotations, an additional 5 mL of SiO_2 suspension was applied, repeating the process 3–5 times to achieve high-quality speckles. The samples were then subjected to in-situ tensile testing in the SEM. DIC and EBSD data were processed using VIC-2D and Channel 5 software, respectively. XRD spectra were collected using Cu-Kα radiation, scanned over a 2θ range of 20°–90° at 5°/min. Before scanning, samples were polished with 200–2000 grit silicon carbide paper, followed by SiO_2 suspension polishing. Additionally, elemental distribution in the sintered samples was analyzed using EPMA (JXA-iHP200F, Japan)

4.4. High-energy synchrotron X-ray tomography

The similar densities of TiBw and TA15 lead to nearly identical X-ray attenuation characteristics, making it challenging to distinguish between them using low-energy X-ray tomography. To resolve the spatial distribution of TiB within the matrix, we employed high-energy synchrotron X-ray tomography to scan the TA15-*Si*-TiB composite. The high-energy synchrotron X-ray tomography was performed at the 3W1 beamline of the Beijing Synchrotron Radiation Facility, using a 55 keV monochromatic X-ray beam. Imaging covered a field of view of 1 × 0.7×2 mm^3 at a source-to-object distance of 1.5 m. The acquired imaging data were reconstructed and sliced using Avizo software for detailed analysis.

4.5. In situ tensile synchrotron X-ray diffraction tests

In-situ high-energy X-ray tensile testing was conducted at Beamline BL12SW of the Shanghai Synchrotron Radiation Facility (SSRF). Monochromatic high-energy X-rays with an energy of 88.409 keV, a wavelength of 0.014025 nm, and a beam size of 0.4×0.4 mm^2 were used to capture two-dimensional diffraction patterns in transmission geometry. The diffraction patterns were acquired using an IRAY 1717V detector with a pixel size of 139×139 μm^2. The sample-to-detector distance, calibrated using a CeO_2 powder standard, was set to 1500 mm and remained consistent across all measurements. The tensile tests were performed on dog bone-shaped samples with nominal gauge dimensions of 10 mm (length) × 3 mm (width)× 1 mm (thickness), loaded using the STEPLAB-UD040 system. Strain-controlled loading was applied at a rate of $0.5\times 10^{-4}\ s^{-1}$, with a pre-load of 200 N applied prior to testing to eliminate equipment gaps. A schematic of the in-situ high-energy XRD tensile setup is shown in the inset of Fig. 2f.

One-dimensional XRD line spectra were generated using the FIT two-dimensional GSAS-II software, with diffraction peaks fitted to a Gaussian distribution. The two-dimensional diffraction patterns were converted into one-dimensional high-energy XRD spectra by caking and integrating over a ±5° range along specified azimuth angles. To calculate the intensity-2θ diffraction spectra for the loading direction (LD), 10° cake segments at positions 0° (360°)±5° (up) and 180°±5° (down) were utilized. This approach improves counting statistics and minimizes the influence of fitting uncertainties.

Currently, calculating dislocation density in HCP (hexagonal close-packed) structures is inherently complex due to the lack of a mature and universally established methodology. In this study, the Williamson–Hall (W-H) method was employed primarily to provide a qualitative assessment of the dislocation density evolution. Using the Williamson–Hall method, dislocation density is calculated from the broadening of diffraction peaks under different strain levels. The broadening of diffraction peaks arises from two main contributions: the average grain size (D) and strain-induced broadening (ε). The relationship between the average grain size and strain is typically expressed by the following equation [48,53,54]:

$$B\cos\theta_{hkil} = K\lambda/D + \varepsilon\sin\theta_{hkil}$$

where B is the XRD peak broadening (full width at half maxima), K is a constant 1, λ is the wavelength of the diffraction, D is the average crystallite size and θ_{hkil} is the Bragg angle of the diffraction peak used for the calculation. The values of D and ε at every applied strain can be calculated by the intercept and slope from the linearly-fitted lines of $B\cos\theta_{hkil}$ as a function of $\sin\theta_{hkil}$.

For each tensile data point, a minimum of four diffraction peaks were used for the calculation. The values of ε and D were determined from the slope of the W-H plot. These values were then substituted into the following formula to estimate the dislocation density. The dislocation density (ρ) can be determined by the following equation:

$$\rho = 2\sqrt{3}\varepsilon/(D^*|\boldsymbol{b}|)$$

Where $\boldsymbol{b}$ is the Burgers vector of the dislocation. Unlike cubic crystals, the plastic deformation of HCP alloys is anisotropic. The three fundamental Burgers vectors of HCP alloys are listed in Table S7. Specifically, b_1=1/3 <1120> (Type <a>) dislocations, b_2=1/3 <0001> (Type <c>) dislocations, and b_3=1/3 <1123> (Type <c+a>) dislocations. The magnitudes of these Burgers vectors for HCP titanium are 0.295 nm (Type <a>), 0.468 nm (Type <c>), and 0.553 nm (Type <c+a>) dislocations. The influence of <c> and <c+a>-type dislocations on diffraction peaks can be neglected due to the significantly higher density of <a>-type dislocations compared to <c> and <c + a> dislocations in the TA15-*Si*-TiB composite. Therefore, in this study, the dislocation density was calculated considering only <a>-type dislocations. Although the contribution of <c+a>-type dislocations to the overall

dislocation density is minimal, <a+c> dislocations play a crucial role in the sustained strengthening and hardening of the material, as they can induce strain along the <c> axis [40,42].

CRediT authorship contribution statement

Shaolong Li: Writing – original draft, Visualization, Methodology, Formal analysis, Data curation, Conceptualization. **Shufeng Li:** Writing – review & editing, Supervision, Funding acquisition, Conceptualization. **Huiying Liu:** Methodology. **Lei Liu:** Conceptualization. **Shaodi Wang:** Methodology. **Dongxu Hui:** Visualization. **Jie Yan:** Investigation. **Rui zhou:** Formal analysis. **Dingbo Tao:** Data curation. **Wenfei Huang:** Investigation. **Jianbo Gao:** Resources, Funding acquisition. **Xiaodong Hou:** Supervision, Data curation. **Xin Zhang:** Supervision, Project administration. **Bo Li:** Resources, Data curation. **Zhimao Wang:** Software. **Gang Li:** Supervision, Conceptualization. **Junhua Luan:** Visualization, Data curation. **Junko Umeda:** Investigation. **Katsuyoshi Kondoh:** Project administration, Formal analysis. **Philip J. Withers:** Writing – original draft, Formal analysis. **Yuntian Zhu:** Writing – original draft, Resources, Project administration, Funding acquisition, Conceptualization.

Data and materials availability

The further source data (>200 GB) that support the findings of this study are available from the corresponding authors upon request.

Declaration of competing interest

The authors declare that they have no known competing financial interests or personal relationships that could have appeared to influence the work reported in this paper.

Appendix A. Supplementary data

Supplementary data to this article can be found online at https://doi.org/10.1016/j.apmate.2025.100369.

References

[1] A. Jarvis, P.M. Forster, Estimated human-induced warming from a linear temperature and atmospheric CO_2 relationship, Nat. Geosci. 17 (12) (2024) 1222–1224.
[2] Y. Zhu, Creating multifunctionality with hierarchical heterostructures, Mater. Res. Lett. 13 (3) (2025) 175–178.
[3] D. Raabe, C.C. Tasan, E.A. Olivetti, Strategies for improving the sustainability of structural metals, Nature 575 (7781) (2019) 64–74.
[4] G. Chen, Y. Peng, G. Zheng, Z. Qi, M. Wang, H. Yu, C. Dong, C.T. Liu, Polysynthetic twinned TiAl single crystals for high-temperature applications, Nat. Mater. 15 (8) (2016) 876–881.
[5] F. Wang, M. Song, M.N. Elkot, N. Yao, B. Sun, M. Song, Z. Wang, D. Raabe, Shearing brittle intermetallics enhances cryogenic strength and ductility of steels, Science 384 (6699) (2024) 1017–1022.
[6] F.K. Yan, Y. Wang, W.J. Lu, X.Y. Li, Nanolamellar and ultrafine equiaxed (α+β) phase heterogeneously architected by nanotwins in a twinning-induced plasticity Ti-12Mo alloy, Acta Mater. 288 (2025) 120844.
[7] Y.H. Zhou, J.Y. Zhang, J. Zhang, X.Y. Yao, J.H. Luan, Q. Li, S.F. Liu, B. Xiao, J. Ju, S.J. Zhao, Y.L. Zhao, Z.Y. Sun, H. Nan, M. Yan, T. Yang, A strong-yet-ductile high-entropy alloy in a broad temperature range from cryogenic to elevated temperatures, Acta Mater. 268 (2024) 119770.
[8] P. Qu, W. Yang, C. Liu, J. Qin, Q. Wang, J. Zhang, L. Liu, Tensile deformation dominated by matrix dislocations at intermediate temperatures revealed using in-situ EBSD in superalloys, Mater. Res. Lett. 12 (2) (2024) 116–124.
[9] L. Liu, S. Li, D. Pan, D. Hui, X. Zhang, B. Li, T. Liang, P. Shi, A. Bahador, J. Umeda, K. Kondoh, S. Li, L. Gao, Z. Wang, G. Li, S. Zhang, R. Wang, W. Chen, Loss-free tensile ductility of dual-structure titanium composites via an interdiffusion and self-organization strategy, Proc. Natl. Acad. Sci. U.S.A 120 (28) (2023) e2302234120.
[10] L.J. Huang, L. Geng, H.X. Peng, Microstructurally inhomogeneous composites: is a homogeneous reinforcement distribution optimal? Prog. Mater. Sci. 71 (2015) 93–168.
[11] T. Song, Z. Chen, X. Cui, S. Lu, H. Chen, H. Wang, T. Dong, B. Qin, K.C. Chan, M. Brandt, X. Liao, S.P. Ringer, M. Qian, Strong and ductile titanium–oxygen–iron alloys by additive manufacturing, Nature 618 (7963) (2023) 63–68.
[12] Y. Zhu, K. Zhang, Z. Meng, K. Zhang, P. Hodgson, N. Birbilis, M. Weyland, H. L. Fraser, S.C.V. Lim, H. Peng, R. Yang, H. Wang, A. Huang, Ultrastrong nanotwinned titanium alloys through additive manufacturing, Nat. Mater. 21 (11) (2022) 1258–1262.
[13] L. Huang, Q. An, L. Geng, S. Wang, S. Jiang, X. Cui, R. Zhang, F. Sun, Y. Jiao, X. Chen, C. Wang, Multiscale architecture and superior high-temperature performance of discontinuously reinforced titanium matrix composites, Adv. Mater. 33 (6) (2021) e2000688.
[14] I. Dowding, C.A. Schuh, Metals strengthen with increasing temperature at extreme strain rates, Nature 630 (8015) (2024) 91–95.
[15] K. Lu, L. Lu, S. Suresh, Strengthening materials by engineering coherent internal boundaries at the nanoscale, Science 324 (5925) (2009) 349–352.
[16] G. Singh, U. Ramamurty, Boron modified titanium alloys, Prog. Mater. Sci. 111 (2020) 100653.
[17] X. Bai, H. Xie, X. Zhang, D. Zhao, X. Rong, S. Jin, E. Liu, N. Zhao, C. He, Heat-resistant super-dispersed oxide strengthened aluminium alloys, Nat. Mater. 23 (6) (2024) 747–754.
[18] Y. Zhu, X. Wu, Heterostructured materials, Prog. Mater. Sci. 131 (2023) 101019.
[19] X. Wu, M. Yang, F. Yuan, G. Wu, Y. Wei, X. Huang, Y. Zhu, Heterogeneous lamella structure unites ultrafine-grain strength with coarse-grain ductility, Proc. Natl. Acad. Sci. U.S.A 112 (47) (2015) 14501–14505.
[20] P. Shi, R. Li, Y. Li, Y. Wen, Y. Zhong, W. Ren, Z. Shen, T. Zheng, J. Peng, X. Liang, P. Hu, N. Min, Y. Zhang, Y. Ren, P.K. Liaw, D. Raabe, Y.D. Wang, Hierarchical crack buffering triples ductility in eutectic herringbone high-entropy alloys, Science 373 (6557) (2021) 912–918.
[21] Q. Pan, L. Zhang, R. Feng, Q. Lu, K. An, A.C. Chuang, J.D. Poplawsky, P.K. Liaw, L. Lu, Gradient cell–structured high-entropy alloy with exceptional strength and ductility, Science 374 (6570) (2021) 984–989.
[22] L. Romero-Resendiz, M. El-Tahawy, T. Zhang, M.C. Rossi, D.M. Marulanda-Cardona, T. Yang, V. Amigó-Borrás, Y. Huang, H. Mirzadeh, I.J. Beyerlein, J. C. Huang, T.G. Langdon, Y.T. Zhu, Heterostructured stainless steel: properties, current trends, and future perspectives, Mater. Sci. Eng., R 150 (2022) 100691.
[23] W. Su, M. Wang, F. Guo, H. Ran, Q. Cheng, Q. Wang, Y. Zhu, X. Ma, C. Huang, Heterostructure enables anomalous improvement of cryogenic mechanical properties in titanium, Acta Mater. 273 (2024) 119982.
[24] X. Dong, B. Gao, L. Xiao, J. Hu, M. Xu, Z. Li, J. Meng, X. Han, H. Zhou, Y. Zhu, Heterostructured metallic structural materials: research methods, properties, and future perspectives, Adv. Funct. Mater. 34 (51) (2024) 2410521.
[25] S. Li, S. Li, L. Liu, H. Liu, C. Wang, P.J. Withers, Y. Zhu, L. Gao, S. Wang, B. Chen, W. Huo, J. Gao, X. Zhang, B. Li, High-temperature "Inverse" Hall-Petch relationship and fracture behavior of TA15 alloy, Int. J. Plast. 176 (2024) 103951.
[26] L. Liu, S. Li, X. Zhang, S. Li, S. Wang, B. Li, L. Gao, H. Liu, D. Hui, D. Pan, S. Kariya, J. Umeda, K. Kondoh, Synthesis mechanism of pelleted heterostructure Ti64-TiB composites via an interdiffusion and self-organization strategy based on powder metallurgy, Compos, Part B 276 (2024) 111366.
[27] Y. Chong, R. Gholizadeh, K. Yamamoto, N. Tsuji, New insights into the colony refinement mechanism by solute boron atoms in Ti-6Al-4V alloy, Scr. Mater. 230 (2023) 115397.
[28] A.K. Singh, C. Ramachandra, Characterization of silicides in high-temperature titanium alloys, J. Mater. Sci. 32 (1) (1997) 229–234.
[29] S. Zhao, R. Zhang, Q. Yu, J. Ell, R.O. Ritchie, A.M. Minor, Cryoforged nanotwinned titanium with ultrahigh strength and ductility, Science 373 (6561) (2021) 1363–1368.
[30] L. Wang, J. Ding, S. Chen, K. Jin, Q. Zhang, J. Cui, B. Wang, B. Chen, T. Li, Y. Ren, S. Zheng, K. Ming, W. Lu, J. Hou, G. Sha, J. Liang, L. Wang, Y. Xue, E. Ma, Tailoring planar slip to achieve pure metal-like ductility in body-centred-cubic multi-principal element alloys, Nat. Mater. 22 (8) (2023) 950–957.
[31] Y. Zhu, K. Ameyama, P.M. Anderson, I.J. Beyerlein, H. Gao, H.S. Kim, E. Lavernia, S. Mathaudhu, H. Mughrabi, R.O. Ritchie, N. Tsuji, X. Zhang, X. Wu, Heterostructured materials: superior properties from hetero-zone interaction, Mater. Res. Lett. 9 (1) (2021) 1–31.
[32] H. Zhang, J. Zhang, J. Hou, D. Zhang, Y. Yue, G. Liu, J. Sun, Making a low-cost duplex titanium alloy ultra-strong and ductile via interstitial solutes, Acta Mater. 241 (2022) 118411.
[33] H. Zhou, C. Huang, X. Sha, L. Xiao, X. Ma, H.W. Höppel, M. Göken, X. Wu, K. Ameyama, X. Han, Y. Zhu, In-situobservation of dislocation dynamics near heterostructured interfaces, Mater. Res. Lett. 7 (9) (2019) 376–382.
[34] L. Li, J. Peng, S. Tang, Q. Fang, Y. Wei, Micromechanism of strength and damage trade-off in second-phase reinforced alloy by strain gradient plasticity theory, Int. J. Plast. 176 (2024) 103970.
[35] H. Gao, Y. Huang, Geometrically necessary dislocation and size-dependent plasticity, Scr. Mater. 48 (2) (2003) 113–118.
[36] H. Gao, Y. Huang, W.D. Nix, J.W. Hutchinson, Mechanism-based strain gradient plasticity— I, Theory, J. Mech. Phys. Solids 47 (6) (1999) 1239–1263.
[37] X. Li, L. Lu, J. Li, X. Zhang, H. Gao, Mechanical properties and deformation mechanisms of gradient nanostructured metals and alloys, Nat. Rev. Mater. 5 (9) (2020) 706–723.
[38] X. Wu, Y. Zhu, Heterogeneous materials: a new class of materials with unprecedented mechanical properties, Mater. Res. Lett. 5 (8) (2017) 527–532.
[39] Y.T. Zhu, X. Liao, Retaining ductility, Nat. Mater. 3 (6) (2004) 351–352.

[40] S. Wei, K.S. Kim, J. Foltz, C.C. Tasan, Discovering pyramidal treasures: multi-scale design of high strength–ductility titanium alloys, Adv. Mater. 36 (33) (2024) 2406382.
[41] Z. Liu, R. Li, D. Chen, Y. Sun, B. He, Y. Zou, Enhanced tensile ductility of an additively manufactured near-α titanium alloy by microscale shear banding, Int. J. Plast. 157 (2022) 103387.
[42] X.W. Zou, W.Z. Han, E. Ma, Uncovering the intrinsic high fracture toughness of titanium via lowered oxygen impurity content, Adv. Mater. 36 (40) (2024) 2408286.
[43] M. Arul Kumar, I.J. Beyerlein, C.N. Tomé, Effect of local stress fields on twin characteristics in HCP metals, Acta Mater. 116 (2016) 143–154.
[44] X.W. Zou, I.J. Beyerlein, W.Z. Han, Hierarchical nanolayered structures-enabled record-high fracture resistant zircaloy, Acta Mater. 279 (2024) 120300.
[45] Y. Lu, Y.H. Zhang, E. Ma, W.-Z. Han, Relative mobility of screw versus edge dislocations controls the ductile-to-brittle transition in metals, Proc. Natl. Acad. Sci. U.S.A 118 (37) (2021) e211059611.
[46] D. An, Y. Xiao, J. Yu, X. Zhang, Z. Li, Y. Ma, R. Li, X. Han, X. Li, J. Chen, S. Zaefferer, The role of dislocation type in the thermal stability of cellular structures in additively manufactured austenitic stainless steel, Adv. Sci. 11 (33) (2024) 2402962.
[47] R. Madec, B. Devincre, L.P. Kubin, From dislocation junctions to forest hardening, Phys. Rev. Lett. 89 (25) (2002) 255508.
[48] Z. An, A. Li, S. Mao, T. Yang, L. Zhu, R. Wang, Z. Wu, B. Zhang, R. Shao, C. Jiang, B. Cao, C. Shi, Y. Ren, C. Liu, H. Long, J. Zhang, W. Li, F. He, L. Sun, J. Zhao, L. Yang, X. Zhou, X. Wei, Y. Chen, Z. Lu, F. Ren, C.T. Liu, Z. Zhang, X. Han, Negative mixing enthalpy solid solutions deliver high strength and ductility, Nature 625 (7996) (2024) 697–702.
[49] D.H. Cook, P. Kumar, M.I. Payne, C.H. Belcher, P. Borges, W. Wang, F. Walsh, Z. Li, A. Devaraj, M. Zhang, M. Asta, A.M. Minor, E.J. Lavernia, D. Apelian, R.O. Ritchie, Kink bands promote exceptional fracture resistance in a NbTaTiHf refractory medium-entropy alloy, Science 384 (6692) (2024) 178–184.
[50] Z. Wu, R. Turner, M. Qi, L. Shi, M. Wang, F. Wang, Z. Gao, Y. Chiu, Z. Zhang, Effect of phase boundary on the critical resolved shear stress and dislocation behavior of dual-phase titanium alloy, Acta Mater. 275 (2024) 120051.
[51] D. Pan, S. Li, L. Liu, X. Zhang, B. Li, B. Chen, M. Chu, X. Hou, Z. Sun, J. Umeda, K. Kondoh, Enhanced strength and ductility of nano-TiBw-reinforced titanium matrix composites fabricated by electron beam powder bed fusion using Ti6Al4V–TiBw composite powder, Addit. Manuf. 50 (2022) 102519.
[52] M. Yang, Y. Pan, F. Yuan, Y. Zhu, X. Wu, Back stress strengthening and strain hardening in gradient structure, Mater. Res. Lett. 4 (3) (2016) 145–151.
[53] J. Ren, Y. Zhang, D. Zhao, Y. Chen, S. Guan, Y. Liu, L. Liu, S. Peng, F. Kong, J. D. Poplawsky, G. Gao, T. Voisin, K. An, Y.M. Wang, K.Y. Xie, T. Zhu, W. Chen, Strong yet ductile nanolamellar high-entropy alloys by additive manufacturing, Nature 608 (7921) (2022) 62–68.
[54] B. Xu, H. Duan, X. Chen, J. Wang, Y. Ma, P. Jiang, F. Yuan, Y. Wang, Y. Ren, K. Du, Y. Wei, X. Wu, Harnessing instability for work hardening in multi-principal element alloys, Nat. Mater. 23 (6) (2024) 755–761.

Shaolong Li is a researcher at Shaanxi Nonferrous Metals Yulin New Materials Group Co., Ltd. He received his Ph.D. degree in Materials Science and Engineering from Xi'an University of Technology. His recent research has focused on the development of heat-resistant titanium matrix composites, the study of strengthening and toughening mechanisms in heterostructured materials, and the research on high-strength and high-toughness aluminum matrix composites.

Shufeng Li is a professor in the School of Materials Science and Engineering at Xi'an University of Technology. He received his Ph.D. degree in Mechanical Engineering from Nihon University, Japan, in 2009. He was a postdoctoral researcher at the Joining and Welding Research Institute (JWRI) of Osaka University. His research focuses on the design and fabrication of metallic (Ti-based, Al-based, etc.) composite powders and their fundamental and applied research in additive manufacturing and powder metallurgy; the strengthening and toughening mechanisms of homogeneous/heterostructured metallic matrix composites; the metallurgical fundamentals and interface control of nano-reinforcements and matrix, and the coordinated strengthening of structural-functional integration for mechanical properties at room/elevated temperatures.

Yuntian Zhu is a chair professor in the Department of Mechanical Engineering and Department of Materials Science and Engineering at the City University of Hong Kong. He received his Ph.D. degree in Materials Science and Engineering from the University of Texas at Austin in 1994. He was a distinguished professor at North Carolina State University from 2007 to 2020. He worked as a postdoc, staff member, and team leader at Los Alamos National Laboratory from 1994 to 2007. His research in recent years has focused on the deformation mechanisms at the dislocation level and mechanical behaviors of heterostructured materials, and nano/ultrafine-grained materials.